

Hot gas around SN 1998bw*

The progenitor inferred through its environment

T. Krühler¹, H. Kuncarayakti^{2,3}, P. Schady¹, J. Anderson⁴, and L. Galbany^{2,3}

¹ Max-Planck-Institut für extraterrestrische Physik, Giessenbachstraße, 85748 Garching, Germany

² Millennium Institute of Astrophysics, Casilla 36-D, Santiago, Chile

³ European Southern Observatory, Alonso de Córdova 3107, Vitacura, Casilla 19001, Santiago 19, Chile

⁴ Departamento de Astronomía, Universidad de Chile, Casilla 36-D, Santiago, Chile

November 14, 2016

ABSTRACT

Spatially-resolved spectroscopy of the environment of explosive transients carries detailed information about the physical properties of the stellar population that gave rise to the explosion, and thus the progenitor itself. Here, we use data from the integral-field spectrograph MUSE of the galaxy hosting GRB 980425 (SN 1998bw) to constrain the stellar population at the explosion site to be consistent with a progenitor of zero-age main-sequence mass between $M_{\text{ZAMS}} \sim 25 M_{\odot}$ and $40 M_{\odot}$ and metallicity $12 + \log(\text{O}/\text{H}) \sim 8.1$ (corresponding to $0.25 Z_{\odot}$). This oxygen abundance is somewhat lower than the one of a nearby H II-region ($12 + \log(\text{O}/\text{H}) \sim 8.3$ or $0.4 Z_{\odot}$) and an integrated measurement over the whole galaxy ($12 + \log(\text{O}/\text{H}) \sim 8.2$ or $0.3 Z_{\odot}$). We demonstrate that simple empirical strong-line methods based on [O III] and/or [N II] are inadequate to produce accurate maps of oxygen abundance as they return gradients in the chemical abundance of individual H II regions, which are not reproduced in their electron-temperature distribution. We show that this behavior is caused by the dependence of these methods on ionization parameter. The metallicity gradient in ESO184-G82 is -0.06 dex per kpc, indicating that the typical offsets of at most few kpc for cosmological GRBs have a small impact for high-redshift measurements on average. Similarly, the GRB/SN site spectrum returns broadly comparable physical parameters than what would be inferred through an unresolved spectrum, typical for high-redshift galaxies.

Key words. Galaxies: star formation

1. Introduction

Line emission from recombination of ionized hydrogen, or decay of collisionally-excited states of metal ions plays a fundamental role in modern astrophysics. The absolute and relative intensities of these transitions crucially depend on the ionizing source, the electron density in the plasma, the ionization state of the elements, and gas-phase abundances (Osterbrock 1989). This makes emission-line spectra of astronomical sources one of the most elementary diagnostics of galaxy formation and evolution (e.g. Tremonti et al. 2004; Erb et al. 2006; Förster Schreiber et al. 2009). The total intensity of the hydrogen recombination lines, for example, is proportional the number of O-type stars, and thus traces the star-formation rate at timescales of ~ 10 Myrs (e.g. Kennicutt 1998). The continuum emission at the wavelength of H α in turn originates from B- or A-type stars, which makes the H α equivalent width (EW) a good tracer of the age of the stellar population.

Metallicity and abundances has been measured through ratios of prominent emission lines from metal ions such as O⁺, O²⁺, N⁺, S⁺ and/or recombination lines of ionized hydrogen (Pagel et al. 1979; Alloin et al. 1979). Given their fundamental importance in galaxy evolution and cosmology, these abundance determinations through nebular emission lines have been the focus of a large body of literature (e.g. Kobulnicky & Kewley 2004; Pilyugin & Thuan 2005; Stasińska 2006; Izotov et al. 2006; Kewley & Ellison 2008).

It is thus immediately clear that an emission-line spectrum of cosmological sources carries detailed information about the underlying stellar population and thus has been used to infer properties not only of galaxies but also of the progenitors of explosive transients. Global (e.g. Prieto et al. 2008; Li et al. 2011) or local (e.g. Anderson et al. 2010; Modjaz et al. 2011; Leloudas et al. 2011) properties of nearby supernovae hosts, as well as cosmological γ -ray bursts (e.g. Wiersema et al. 2007; Krühler et al. 2012; Graham & Fruchter 2013) or super-luminous supernovae (e.g. Chen et al. 2013; Lunnan et al. 2014; Leloudas et al. 2015; Perley et al. 2016) have likewise been used to compare progenitor models with the expected environments.

A fundamental assumption of all these studies is the hypothesis that there is a tight relation between measured gas-phase oxygen abundance of H II regions and progenitor metallicity. Clearly, this link is most robust when coming from an analysis of the co-spatial stellar-population. Integral-field spectroscopy (IFS) with high angular resolution is thus arguably the most comprehensive way of studying the environments of explosive transients. Nearby galaxies hosting supernovae (SN), for example, are hence ideal targets for state-of-the-art integral-field units (IFUs, e.g. Kuncarayakti et al. 2013; Galbany et al. 2014).

In contrast to nearby SNe, the cosmological distances of GRBs (e.g. Fynbo et al. 2009; Krühler et al. 2015) have always posed serious limitations on using IFU spectroscopy for GRB-selected galaxies. Only few GRBs are close enough such that the spatial resolution with modern ground-based instrumentation yields constraints on scales better than a kpc. Seminal work

* Based on observations at ESO, Program ID: 095.D-0172

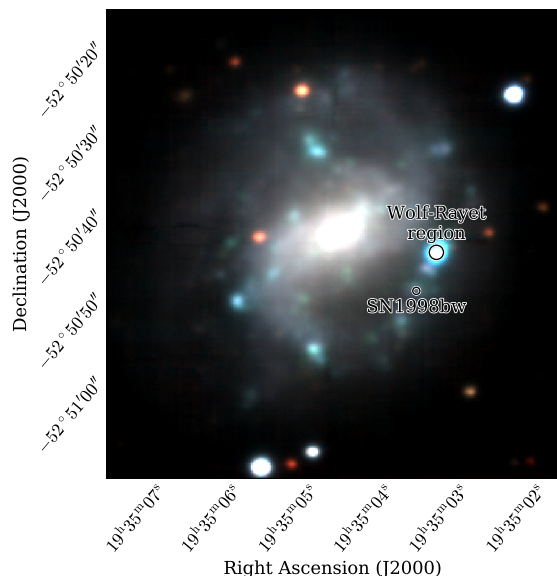


Fig. 1: Reconstructed image from the MUSE data cube. False-color composite from reconstructed *VRI*-band images. The image spans approximately $55''$ by $55''$, or 10 by 10 kpc. One MUSE spaxel corresponds to 35 pc. The effective spatial resolution is given by the point spread function with a FWHM of approximately $0''.9$.

on spatially-resolved spectroscopy for nearby GRB hosts was obtained using long-slit spectroscopy (e.g. Thöne et al. 2008; Levesque et al. 2011; Schady et al. 2015) or the previous generation of IFUs (Christensen et al. 2008; Thöne et al. 2014).

The focus of this article are our new observations of the poster-child of the GRB/SN connection, GRB 980425/SN 1998bw obtained with the Multi-Unit Spectroscopic Explorer (MUSE, Bacon et al. 2010). GRB 980425 is the closest GRB yet discovered and both the GRB (e.g. Galama et al. 1998; Kulkarni et al. 1998), the SN (e.g. Iwamoto et al. 1998; Patat et al. 2001; Maeda et al. 2006) and host galaxy (e.g. Fynbo et al. 2000; Sollerman et al. 2005; Hammer et al. 2006; Michałowski et al. 2009) are extensively discussed in existing literature.

Compared to the bulk of cosmological GRBs, GRB 980425 was rather peculiar: the isotropic-equivalent release in γ -rays of GRB 980425 was $\sim 10^{48}$ erg (Galama et al. 1998), a factor of ten lower than other local, low-luminosity GRBs, or around five orders of magnitudes less than conventional GRBs (Xu et al. 2013). No bright multi-wavelength afterglow was observed for GRB 980425 despite its proximity. Yet, the associated SN with its absence of H and He, broad metal absorption lines and high luminosity has proven to be typical of GRB/SN in general (Hjorth & Bloom 2012).

The host galaxy of GRB 980425/SN1998bw, ESO184-G82 (Lauberts & Valentijn 1989), is a barred spiral dwarf galaxy (Fynbo et al. 2000) seen nearly face on (Figure 1) with a visible extend of approximately $67''$ by $57''$ (12×10 kpc) at the $B = 26.5$ mag isophote (Sollerman et al. 2005). Its brightness, luminosity, and stellar mass are $B = 14.94$ mag, $M_B = -17.65$ mag or $L = 0.05 L^*$, and $\log(M_*/M_\odot) = 8.7$, respectively (Sollerman et al. 2005; Michałowski et al. 2014). SN 1998bw exploded in a H II-region $12''$ distant (2 kpc projected) from its center, 860 pc to the South-East from a young star-forming region which dis-

plays signatures of Wolf-Rayet stars in its spectrum (Hammer et al. 2006), the so-called Wolf-Rayet (WR) region (Figure 1).

Despite the large set of recent literature on GRB 980425 and its host mentioned above, we have decided to summarize our new data and conclusions here mainly because of three reasons: The unique combination of spatial resolution and sensitivity of MUSE helps to clarify some of the ambiguities around SN 1998bw from previous works. The MUSE data provides the best constraints the immediate environment and underlying stellar population of SN 1998bw yet available. And last but possibly most important, it is an informative example of spatially-resolved oxygen-abundance measurements in star-forming galaxies through strong line diagnostics and their dependence on other physical conditions in the interstellar medium.

Throughout the paper, we adopt a Λ CDM cosmology with Planck parameters (Planck Collaboration 2014), a Chabrier (2003) IMF, and report errors at the 1σ confidence level.

2. Observations

We observed ESO184-G82 ($z = 0.0086$, or $D_L = 37$ Mpc in concordance cosmology) using the Multi-Unit Spectroscopic Explorer (MUSE, Bacon et al. 2010) at the VLT on two clear nights starting on 2015-05-14 and 2015-05-15 in a classical observing run from Paranal. In each night, we obtained four dithered exposures of 450 s integration each, totaling 3600 s on source. The on-target frames were supplemented by an offset pointing to blank sky for 200 s. For absolute flux calibration, we observed the spectro-photometric standard LTT3218 at the beginning of each night. The full-width half maximum of the stellar point spread function, which defines our spatial resolution, is between $0''.9$ (at 9000 \AA) and $1''.1$ (at 5000 \AA) in the MUSE data.

The MUSE instrument is a state-of-the-art integral-field spectrograph (IFS), splitting the light into 24 individual and identical subunits. In the wide-field mode, each of these sub-IFU disperses a $60'' \times 2.5''$ region of the sky onto a single CCD. In this way, MUSE covers a continuous sky region of $60'' \times 60''$ in the wavelength range between 4800 \AA and 9300 \AA when operated in its nominal configuration. With its excellent total throughput, small spaxel size ($0''.2 \times 0''.2$), and decent resolving power ($1800 < R < 3600$ increasing from blue to red wavelengths), MUSE offers a unprecedented combination in sensitivity, spatial resolution and field of view for IFUs (Bacon et al. 2010).

3. Data Reduction

We reduced our data with the pipeline supplied through ESO¹ in its version 1.2.1 (Weilbacher et al. 2014), which applies corrections for bias level, flat-fields, illumination level and geometric distortions of MUSE. The ESO pipeline also performs the wavelength calibration using day-time arclamp frames, which is subsequently refined using sky-lines in the science data. The sky background was subtracted using the offset pointing through algorithms from the Zurich Atmospheric Package (Soto et al. 2016). The exposures from the two different nights were then corrected for slight pointing offsets between night one and two and stacked using variance-weighting, and de-reddened based on the Galactic foreground $E_{B-V} = 0.050$ mag (Schlafly & Finkbeiner 2011).

The final data cube has slight offsets between the VLT astrometry and a global astrometric solution, which we correct by

¹<http://www.eso.org/sci/software/pipelines/>

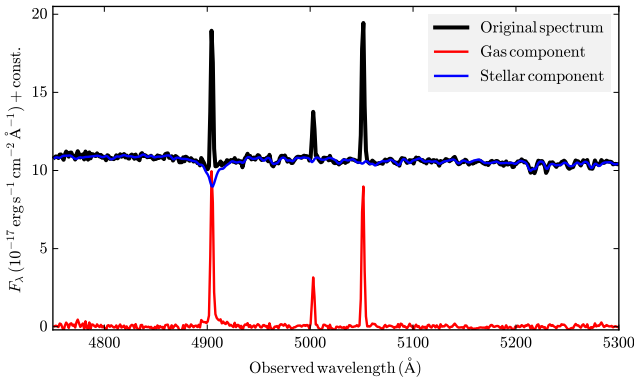


Fig. 2: Separating stellar and gas-phase spectra. This figure shows a zoom-in to the wavelength region around $H\beta$ including the two strong $[O\text{ III}](\lambda\lambda 4959, 5007)$ lines at an arbitrary location from the MUSE cube. Black is the original spectrum, blue the fitted stellar component, and red the resulting spectrum for the gas-phase only. Blue and black spectra are shifted to enhance clarity in the Figure. Note the significant Balmer absorption around $H\beta$.

tying the position of stars in the field of MUSE to coordinates from a reference image taken with the SOFI/NTT on 2000-10-25. We then measure the position of the SN in the reference frame, mapping it onto the MUSE cube with an accuracy of around 50 mas. Figure 1 shows a false-color image reconstructed from the MUSE cube where the position of SN 1998bw is indicated.

In a similar way, we use photometry to corroborate our flux calibration through the V , R_C and I_C -band magnitudes of star 1 of Clocchiatti et al. (2011) yielding differences of 0.05 ± 0.03 mag, 0.05 ± 0.06 mag and 0.00 ± 0.05 mag compared to our MUSE spectrum. After applying a small offset using a linear fit to the photometry-based correction factors, we can accurately reproduce the optical colors of the host galaxy (Sollerman et al. 2005) to better than 0.02 mag.

4. Analysis and Discussion

4.1. Separating Gas-phase and Stellar Component.

As we are primarily interested in the absolute and relative strengths of the nebular lines, and thus the gaseous component of the galaxy, we need to remove the stellar component for accurate line flux measurements, in particular for the Balmer lines. The stellar Balmer absorption has a significant influence on the emission line measurement of $H\beta$ (Figure 2). It is primarily a function of line intensity and age of the underlying stellar population, and thus depends on the position within a galaxy, and needs to be accurately modeled for reliable constraints on the Balmer decrement.

We separate the galaxy’s star and gas components by fitting a linear superposition of template stellar spectra based on the Bruzual & Charlot (2003) models to the MUSE data. We divide the full field of view into regions with a size of $0''.6 \times 0''.6$ (or 3 by 3 spaxels), and extract spectra for each of the ~ 9000 subregions. These spectra are then fit with stellar models using *starlight* (Cid Fernandes et al. 2005, 2009) in a similar fashion as we did elsewhere (Galbany et al. 2016a; Kuncarayakti et al. 2016; Prieto et al. 2016). The 3×3 co-adding effectively is an increase in signal-to-noise at the expense of spatial resolution for the stellar properties, but is necessary to robustly perform an automated fit

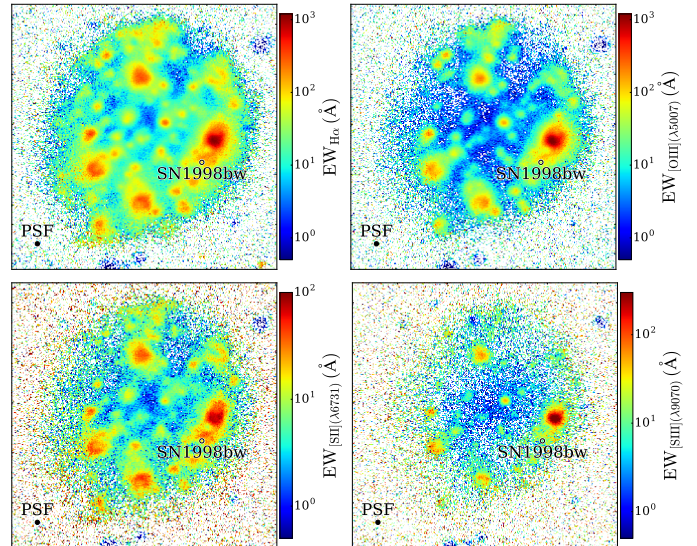


Fig. 3: Reconstructed images from the MUSE data cube. Each panel shows the host of GRB 980425 in a different wavelength regime. Top-left: $H\alpha$, top-right: $[O\text{ III}](\lambda 5007)$, bottom-left: $[S\text{ II}](\lambda 6731)$, bottom-right: $[S\text{ III}](\lambda 9070)$. All panels are approximately $55''$ by $55''$, or 10 by 10 kpc in size. One MUSE spaxel corresponds to 35 pc. The effective spatial resolution is given by the point spread function indicated in the lower left corner of each image with a FWHM of approximately $0''.9$.

in particular in the fainter regions of the galaxy. We then linearly scale the best-fit stellar template to the intensity in single spaxels. Subtracting this stellar component from the original data results into the contribution of the gas-phase only (Figure 2).

4.2. Equivalent Width Maps

After having separated gas-phase and stellar component it is trivial to produce maps of line flux (integral over the gas-phase), continuum (average of the stellar component) and equivalent width (flux over continuum). Figure 3 displays the $H\alpha$ equivalent width map, which is a rather direct proxy of stellar population age, which then can be interpreted as a tracer for progenitor mass. The spaxel closest to the SN/GRB position has an $H\alpha$ equivalent widths of $EW_{H\alpha} = 98 \text{ \AA}$. The spaxels within a radius of 70 pc yield $EW_{H\alpha} = 88 \pm 15 \text{ \AA}$.

Assuming a single stellar population from an instantaneous starburst, this corresponds to stellar-population ages between 5 Myr and 8 Myrs from various models at metallicities of $Z = 0.004$ or $Z = 0.2 Z_{\odot}$ (see e.g. Levesque & Leitherer 2013; Kuncarayakti et al. 2016, and references therein). The relatively large range in ages is almost entirely due to the spread from different stellar evolution models or initial mass functions. These ages corresponds to life-times of stars with zero-age main sequence masses (ZAMS) of approximately 25 to 40 M_{\odot} (Fagotto et al. 1994; Meynet & Maeder 2005), which is similar to the one derived by modeling the SN 1998bw nebular spectra of $M_{ZAMS} \gtrsim 30 - 35 M_{\odot}$ (Mazzali et al. 2001; Maeda et al. 2006), or found previously from host spectra (Sollerman et al. 2005).

These considerations are only valid, of course, if the progenitor was born where it exploded, and was not ejected from the nearby WR region (Hammer et al. 2006). However, the WR region is so young such that timing arguments make this scenario contrived: Very high EW values of $H\alpha$ and nebular transi-

tions are observed in the center of the WR-region (both $EW_{H\alpha}$ and $EW_{[O III](\lambda 5007)} > 1000 \text{ \AA}^2$). Together with the detection of strong $He I(\lambda 4922)$, they indicate population ages of smaller than 3 Myr (see also Sect. A) in instantaneous star-burst models, or $M_{ZAMS} \gtrsim 60 M_{\odot}$ (see e.g. Thöne et al. 2015, and references therein). The discrepancy with respect to the progenitor mass from SN modeling then suggests, that the GRB progenitor was indeed not born in the WR-region, but rather formed in situ.

For a travel time shorter than the age of the WR region ($< 3 \text{ Myr}$), the required peculiar velocities v are extremely high ($v > 260 \text{ km s}^{-1}$). This is a strict lower limit, as projection effects further increase the required velocities. Scenarios that are believed to give rise to these kind of massive runaway stars are dynamical few-body encounters or binary supernovae, but both seem unfeasible here: A dynamical ejection produces hyper-velocity stars in only very rare and extreme cases (Hoogerwerf et al. 2001; Perets & Šubr 2012), and the probability of potential GRB progenitors ($M_{ZAMS} \gtrsim 20 M_{\odot}$) getting velocity kicks with $> 200 \text{ km s}^{-1}$ from a companion SN is also practically zero (El-dridge et al. 2011). This makes a binary supernova origin highly implausible as there would just not be enough time to evolve and explode the primary and eject the secondary to a distance $\gtrsim 860 \text{ pc}$. Also the fraction of ejected stars by dynamical encounters is of course a function of the elapsed time, and reaches only 0.01/0.03 at 1 or 3 Myr at $M_{ZAMS} \sim 35 M_{\odot}$ (Banerjee et al. 2012), again leaving little time for the ejected star to travel as far as 860 pc (or further).

Given the presence of massive stars in the vicinity of the SN position (Fynbo et al. 2000), the substantial level of recent star-formation as evidenced through high EW of nebular lines at the SN position (Figure 3), and the consistency between M_{ZAMS} derived from the age of the stellar population as well as the SN 1998bw nebular spectra, we see no compelling reason to invoke an artificial ejection from the nearby H II-region region to explain the GRB location within its host.

4.3. Dust Distribution

Due to its exquisite photometric and spectroscopic data set, SN1998bw is a widely-used comparison object, so it is fundamental to quantify the absorbing dust to derive its intrinsic properties. To this end, we convert our line fluxes of $H\alpha$ and $H\beta$ into a map of color-excess E_{B-V} as shown in Figure 4 using Equation 5 of Krühler et al. (2015). This procedure assumes standard ratios of the Balmer lines at 10^4 K and $n_e \sim 100 \text{ cm}^{-3}$ from Osterbrock (1989), broadly consistent with the values obtained for this galaxy (Table 1), and depends only marginally on the extinction law, as the difference between reddening laws in the local group is small in the wavelength range probed by $H\alpha$ and $H\beta$.

Figure 4 shows very little dust in general in ESO184-G82, and also only minor evidence for dust at the actual GRB/SN position ($E_{B-V} = 0.06 \text{ mag}$, or $A_V = 0.19 \text{ mag}$) and its immediate environment $E_{B-V} = 0.03^{+0.06}_{-0.03} \text{ mag}$ in the 9 spaxels closest to the GRB/SN position). The only location where we observe evidence for significant dust reddening are the centers of H II regions as exemplified by the WR-region, which shows a centrally-symmetric substructure in dust extinction decreasing from the inside out peaking at $E_{B-V} \sim 0.25 \text{ mag}$ or $A_V = 0.8 \text{ mag}$. A

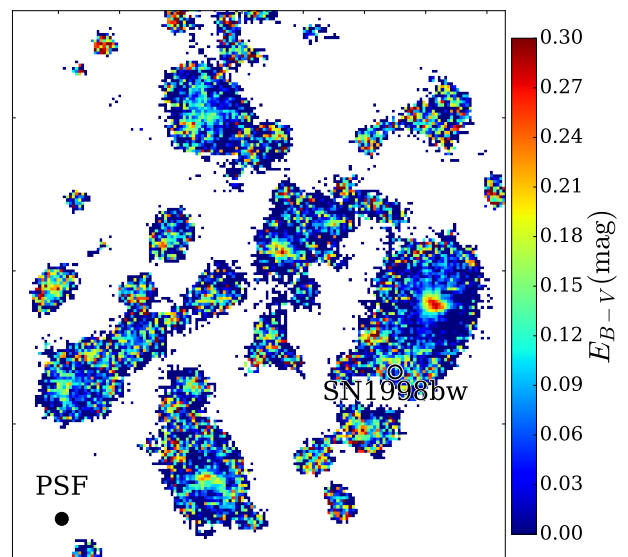


Fig. 4: Dust distribution in ESO184-G82 as measured through the Balmer decrement. We only show spaxels in which $H\beta$ is detected with a significance of at least 3σ . The shown image spans $34''$ by $38''$, or 6.1 by 6.8 kpc . The circle denoting the position of SN 1998bw has a radius of 180 pc .

galaxy-integrated spectrum yields $E_{B-V} = 0.05 \pm 0.02 \text{ mag}$, or $A_V = 0.15 \pm 0.06 \text{ mag}$, which is in remarkable agreement with the average optical depth τ_V derived from modeling the UV-to-radio SED (Michałowski et al. 2014).

Our new data thus resolve the apparent conflict with the unexpectedly large reddening at the SN position derived from previous spectroscopic data (Hammer et al. 2006; Christensen et al. 2008) and the SN itself, which did not show any evidence of strong dust obscuration (e.g. Iwamoto et al. 1998; Patat et al. 2001). They provide further confidence in using SN 1998bw as an only very mildly reddened SN template for comparison to other GRB/SNe (e.g. Zeh et al. 2004; Kann et al. 2016, and numerous references therein).

4.4. Metallicity Diagnostics

4.4.1. Initial considerations

Metal abundances in H II regions are a central observable to study cosmo-chemical evolution, and a large set of literature is devoted to the various possibilities, their advantages, and perils to infer abundances from H II-region spectra (e.g. Pagel et al. 1979; McGaugh 1991; Pilyugin & Thuan 2005; Kewley & Ellison 2008). Very briefly, the most common methods to infer chemical abundances, and from those, the abundance of oxygen (traditionally expressed in $12 + \log(O/H)$) make use of either photo-ionization models (e.g. Evans & Dopita 1985; Dopita et al. 2000; Kewley & Dopita 2002) or empirical correlations between certain strong-line ratios and oxygen abundances derived through electron temperatures T_e from collisionally-excited lines (CELs, e.g. Pettini & Pagel 2004; Marino et al. 2013). Commonly used ratios are for example $[N II]/[O II]$, $[O III]/[N II]$, $[N II]/H\alpha$, or $R_{23} = ([O II] + [O III])/H\beta$, which have been (re)-calibrated numerous times against different samples of T_e or photo-ionization models, yielding a large set of different calibrators in the literature (e.g. Kewley & Dopita 2002; Kobulnicky & Kewley 2004; Pilyugin & Thuan 2005; Nagao et al. 2006; Maiolino et al. 2008).

²These are strictly lower limits. The fact that the compact WR-region is convolved with the seeing-introduced spatial scale of $\sim 0.9''$ leads to a smoothed EW distribution. In fact, the FORS2 data discussed in Appendix Sect. A were taken under significantly better atmospheric conditions and show EW values around 2000 \AA

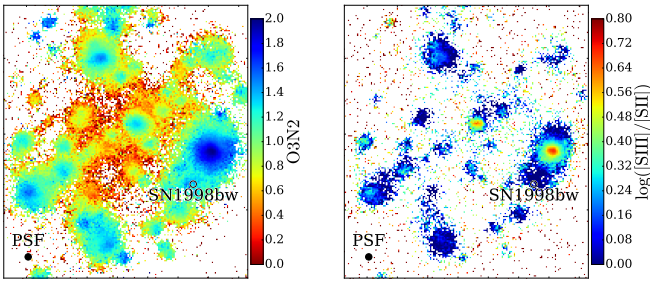


Fig. 5: Face-to-face comparison between the maps of O3N2, often used for abundance determinations and $[S\text{ III}]/[S\text{ II}]$, a tracer of the ionization state of the hot gas. Only spaxels with SNR > 3 are shown. Image dimensions are similar to Figure 4.

One of the fundamental problems in using and interpreting the oxygen abundances derived in this way is that different methods are only very rarely consistent (e.g. Kewley & Ellison 2008) giving rise to the abundance determination problem (Peimbert 1967). Methods based on temperature-sensitive collisionally-excited lines typically show abundances that are lower by 0.2-0.4 dex with respect to photoionization-based methods or abundances derived using temperatures from recombination lines (e.g. López-Sánchez et al. 2012, and references therein), in particular in the high-metallicity region. A possible solution to the abundance determination problem are small-scale temperature fluctuations (e.g. Peimbert 2003; Esteban et al. 2004) or an electron population distributed somewhat differently than in thermal Maxwell-Boltzmann equilibrium (Nicholls et al. 2012; López-Sánchez et al. 2012), but until these discrepancies are fully resolved, element abundances from emission lines remain the subject of controversy.

A second, independent problem relates to the observational difficulties in robustly measuring emission line fluxes for lines in different wavelength ranges for faint, high-redshift galaxies. Due to various observational constraints, the available data is typically limited to a handful of strong lines. This is similarly true for our observations, as the MUSE data do not cover neither the strong $[O\text{ II}](\lambda\lambda 3726, 3729)$ doublet nor $[O\text{ III}](\lambda 4363)$, one of the most commonly-used, temperature-sensitive CEL. A very popular emission-line diagnostic in the literature has thus been the logarithm of the ratio of $[O\text{ III}]/H\beta$ to $[N\text{ II}]/H\alpha$ or short O3N2 (e.g. Pettini & Pagel 2004; Marino et al. 2013), because of its independence on dust reddening and relative observational ease with which it can be measured even at $z \sim 2$.

4.4.2. Specific Problems of Empirical Metallicity Diagnostics

Yet, from the very different ionization potentials of N and O^+ , it is immediately clear that O3N2 also carries a strong dependence on the ionization parameter in addition its inverse proportionality with oxygen abundance (e.g. Alloin et al. 1979; Ho et al. 2015). In Figure 5, we plot the O3N2 map, which would immediately translate into a map of oxygen abundance, ($12 + \log(O/H)$ would be lowest where O3N2 is highest) in common diagnostics (Pettini & Pagel 2004).

However, when inspecting the left part of Figure 5 it becomes apparent that O3N2-based oxygen abundances (and similarly for those based on N2) would produce abundance maps that are hard to explain in a physical context: O3N2 varies significantly on \lesssim

kpc scales, and would lead to an unexpected³, chemically inhomogeneous structure within individual H II regions with their central abundances up to 0.3 dex lower than their outer edges. However, we believe that the significant gradients in O3N2/N2 observed in most of our H II regions are unlikely due to a genuine gradient in oxygen abundance but more likely the effect of a changing ionization parameter on O3N2/N2. We will explore this hypothesis further in the following sections.

4.4.3. Ionization Maps

Our MUSE data is of sufficient depth and quality to test how strongly O3N2 is affected by ionization empirically through the ratio of $[S\text{ III}](IP=23.3\text{ eV})$ to $[S\text{ II}](IP=10.3\text{ eV})$, widely considered as one of the best tracers of the ionization parameter (Diaz et al. 1991) as it shows in contrast to $[O\text{ III}]/[O\text{ II}]$ only very little dependence on abundance itself (Kewley & Dopita 2002; Dors et al. 2011). The resulting map⁴ is shown in Figure 5 and clearly highlights the H II region centers standing out with the largest values of $[S\text{ III}]$, and thus ionization parameter.

This adds further support to our initial conjecture, and attributes the radial symmetric structure of individual H II-regions in the O3N2 and N2 maps to an increase of the ionization parameter towards the center of H II regions and not chemical inhomogeneities. Simple O3N2, or N2-based diagnostic are thus inadequate to produce accurate maps of oxygen abundance at the level of detail of our MUSE data (see also Sect. B).

4.4.4. Metallicity Maps

After rejecting empirical methods using O3N2 or N2 as reliable metallicity tracer due to their ionization dependence, we turn to diagnostics based on photo-ionization models. Unfortunately, most of the previous strong-line methods rely in one way or another on the strong $[O\text{ II}](\lambda\lambda 3726, 3729)$ doublet (Kewley & Dopita 2002), which is not directly available to us here. Also $[S\text{ III}]/[S\text{ II}]$ is a good ionization tracer, but $[S\text{ III}]$ is relatively faint and not detected in most of our spaxels (see Figure 5). A recently published method based on photo-ionization modeling (Dopita et al. 2016) seems to perfectly fit to our data. It relies solely on $H\alpha$, $[N\text{ II}]$, and $[S\text{ II}]$, which are all strong and well within the wavelength range of MUSE. The method is introduced as "effectively independent of both ionization parameter and ISM pressure" (Dopita et al. 2016), and Figure 6 displays the respective map of $12 + \log(O/H)$ in regions where the necessary lines are detected at sufficient SNR.

Clearly, the strong abundance gradient over individual H II-regions as would have been deduced from O3N2, is not observed in this diagnostic. Instead, the oxygen abundance map displays a relatively smooth behavior with a decreasing overall metallicity from the center of the galaxy towards the outside (see also Sect. 4.5). The spaxel abundance at the SN position is $12 + \log(O/H) = 8.00$ or $0.20 Z_{\odot}$. The immediate environment is consistent with this value and relatively homogeneous: within a radius of 70 pc to the SN position $12 + \log(O/H)$ is 8.06 ± 0.06 . The WR region displays a somewhat higher metallicities with

³Despite the filamentary structure of nearby giant H II regions like 30 Doradus, they are usually adequately described with abundances that are homogenous throughout the region (e.g. Pellegrini et al. 2011, and references therein).

⁴As MUSE does not cover the wavelength range of $[S\text{ III}](\lambda 9532)$, we use a theoretical value of $[S\text{ III}](\lambda 9532) = 2.44 \times [S\text{ III}](\lambda 9069)$ (Mendoza & Zeippen 1982) here.

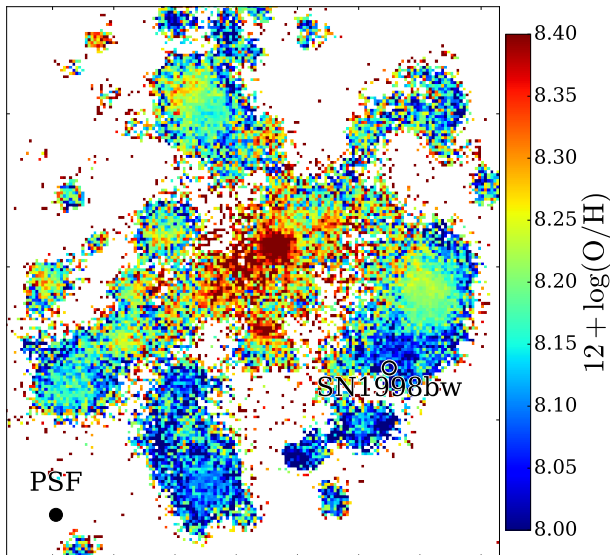


Fig. 6: Map of $12 + \log(\text{O}/\text{H})$ as obtained through the $[\text{S II}]$ and $[\text{N II}]$ based calibration of Dopita et al. (2016). Only spaxels with $\text{SNR} > 3$ are shown. Image dimensions are $34''$ by $38''$, or 6.1 kpc by 6.8 kpc, similar to Figure 4. The circle denoting the position of SN 1998bw has a radius of 180 pc. Abundance determination methods via lines that are sensitive to electron temperature return 0.1 - 0.2 dex values.

the oxygen abundances of at the peak of the $\text{H}\alpha$ emission yielding $12 + \log(\text{O}/\text{H}) = 8.21 \pm 0.03$ or $0.33 \pm 0.03 Z_{\odot}$.

It is of course reasonable to ask now whether the new Dopita et al. (2016) diagnostic provides more reliable constraints on oxygen abundance than previous methods given the significant differences when compared to abundances derived in previous works. In addition, for low-mass galaxies as is the case here, this diagnostic seems to return lower oxygen abundances than previous methods (Kashino et al. 2016). To elaborate further on the $[\text{S II}]$ -based diagnostic, we reproduce Equation 1 and 2 from Dopita et al. (2016)

$$12 + \log(\text{O}/\text{H}) = 8.77 + \log([\text{N II}]/[\text{S II}]) + 0.264 \log([\text{N II}]/\text{H}\alpha) \quad (1)$$

with $[\text{N II}]$ being the flux in the $[\text{N II}](\lambda 6484)$ line, and $[\text{S II}]$ the flux in the $[\text{S II}](\lambda \lambda 6717, 6731)$ doublet. The primary observable is thus the nitrogen to sulfur ratio, which is a tracer of the nitrogen to oxygen ratio⁵. Because nitrogen is also produced in intermediate mass stars, N/O starts to depend on $12 + \log(\text{O}/\text{H})$ above $12 + \log(\text{O}/\text{H}) \sim 7.8$ (e.g. Izotov & Thuan 1999; Pérez-Montero et al. 2013), and as expected, a N/O map via Amorín et al. (2010) is very similar to the map of oxygen abundance in the respective strong line diagnostic.

The map of oxygen abundance then fundamentally relies on the N/O-to-O/H, calibration, and it is in principle not impossible that the applied calibration is somewhat offset, in particular in the low-metallicity region. There could also be internal variations in N/O at a given $12 + \log(\text{O}/\text{H})$, or differences between the host of SN 1998bw to the calibration sample. For example infall of primordial gas would decrease $12 + \log(\text{O}/\text{H})$, but leave

⁵Sulfur and oxygen are both α -process elements produced in massive stars, and observed to track each other well in different environments (see e.g. Figure 6 in Izotov et al. 2006).

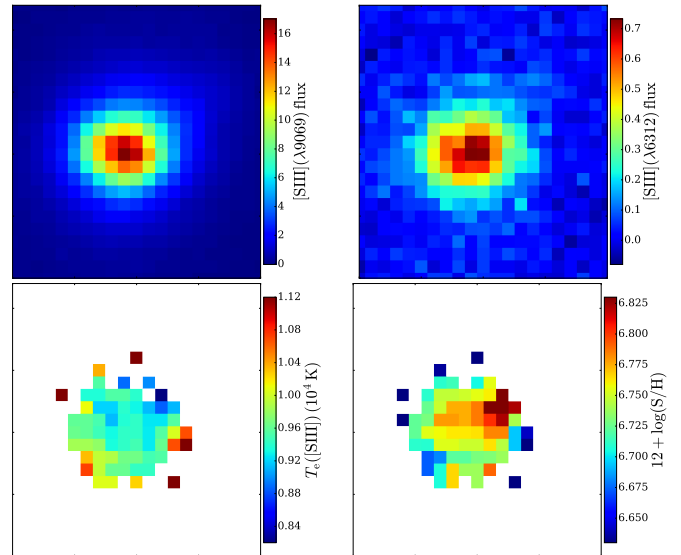


Fig. 7: Zoom-in to the WR region for temperature estimation. top-left: nebular $[\text{S III}](\lambda 9069)$, top-right: auroral $[\text{S III}](\lambda 6312)$, bottom-left: $[\text{S III}]$ electron temperatures, bottom-right: $12 + \log(\text{S}/\text{H})$ as derived from the electron temperature. The solar abundance $[\text{O}/\text{S}]$ is 1.57 (Asplund et al. 2009), so the $12 + \log(\text{S}/\text{H})$ scale corresponds to $12 + \log(\text{O}/\text{H}) = 8.2$ to 8.4 . All panels are approximately $6''$ by $6''$, or 1 by 1 kpc. One MUSE spaxel corresponds to 35 pc.

N/O unaffected (Kashino et al. 2016). Another point of concern would be an anomalously high N/O ratio for the SN region as claimed in Hammer et al. (2006). However, both of these effects would lead us to over predict the actual oxygen abundance in the SN region, whereas we observe some of the lowest values here. Also the calibration sample for N/O-to-O/H in the metallicity range of interest is based on low-metallicity blue compact dwarf galaxies (Izotov & Thuan 1999), not dissimilar in physical properties to our galaxies.

4.4.5. Metallicities Based on Electron Temperatures

Given the strong constraints that these measurements of oxygen abundance imply for the SN 1998bw progenitor, we further seek to corroborate our earlier metallicities through those from temperature-sensitive lines. Unfortunately, the brightest of those ($[\text{O III}](\lambda 4363)$) is not covered by the MUSE wavelength response, and the other temperature-sensitive lines are too faint to be detected in most of the individual spaxels. However, we clearly detect both $[\text{S III}](\lambda 6312)$ in the WR region (Figure 7), and in a integrated spectrum from spaxels within a radius of $0''.8$ around the SN position.

Following Nicholls et al. (2013), we derive an electron temperature $T_{\text{me}}^{\text{[S III]}}$ using $[\text{S III}]$ in the central part of the WR-region of around $T(e)_{[\text{S III}]} = (0.94 \pm 0.04) \cdot 10^4$ K. Figure 7 contains maps of the crucial emission lines (nebular $[\text{S III}](\lambda 9069)$, and auroral $[\text{S III}](\lambda 6312)$), the resulting temperatures as well as sulfur abundances. These values correspond to somewhat larger temperatures of $[\text{O III}]$ of around $T(e)_{[\text{O III}]} \sim 1.07 \cdot 10^4$ K (Izotov et al. 2006; Binette et al. 2012). The flux in the doublets of $[\text{O II}](\lambda \lambda 7320, 7330)$ and $[\text{O III}](\lambda \lambda 4959, 5007)$ then yields central abundances of the WR region around $12 + \log(\text{O}/\text{H}) \sim 8.3$.

Similar values are obtained when using solar abundances to convert the sulfur to an oxygen abundance. These are somewhat

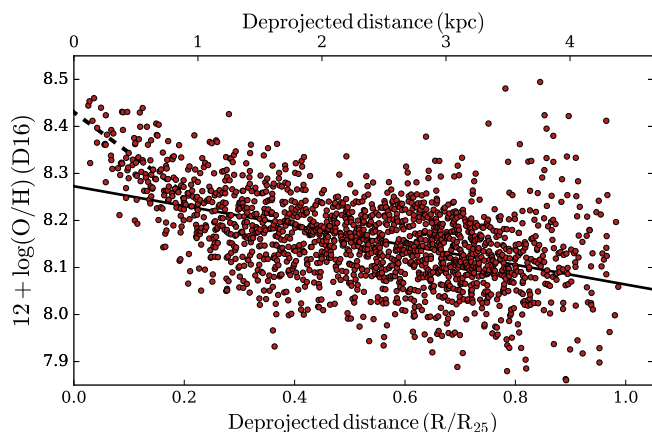


Fig. 8: Metallicity gradient.

(0.1–0.2 dex.) higher than those implied by the strong line diagnostic from Sect. 4.4.4, but critically depend on the sulfur-to-oxygen temperature conversion or assumed abundance. They are thus subject to some systematic uncertainties. However, it is clear that the strong structure in O3N2 or N2 over the H β -region are not observed in electron temperatures.

Emission-lines in the SN region are substantially fainter, and [S III]($\lambda 6312$) is only detected in a stacked spectrum extracted from 3x3 spaxels around the SN position yielding $T_e([S\text{ III}]) = (1.24 \pm 0.18) \cdot 10^4$ K, slightly higher than in the WR-region, but with large uncertainties.

We also re-reduce archival VLT/FORS2 long-slit spectroscopy (Sect. A) as it covers both WR-region and SN position and extends below 4000 Å. Using the well-detected [O III]($\lambda 4363$) line, we measure temperatures of $T_e([O\text{ III}]) = (1.05 \pm 0.05) \cdot 10^4$ K and $T_e([O\text{ III}]) = (1.29 \pm 0.18) \cdot 10^4$ K for the WR and SN region, respectively, broadly consistent with the estimates from MUSE through [S III]($\lambda 6312$). They imply oxygen abundances of $12 + \log(O/H) = 8.36 \pm 0.07$ and 8.09 ± 0.15 for WR and SN region respectively.

Our relatively low oxygen abundances at the location of SN ($12 + \log(O/H) \sim 8.1$ – 8.2) and WR-region ($12 + \log(O/H) \sim 8.3$ – 8.4), as well as galaxy integrated values (~ 8.2 – 8.3) correspond to 0.2 to 0.4 times the solar value, and thus explain many of the long-wavelength properties of ESO184-G82 as typical for metal poor dwarf galaxies without invoking a deficiency in molecular gas (Michałowski et al. 2016).

4.5. Metallicity Gradients

The metallicity of galaxies is often observed to decrease with the distance from their centers (e.g. Zaritsky et al. 1994; Sánchez et al. 2014), also observed in the hosts of SNe (Galbany et al. 2016b). These gradients are important to understand for spatially-unresolved studies at high redshift, where positional offsets can be measured, but abundances are only derived in a galaxy integrated manner. From Figure 6, it is immediately clear that we are observing a similar effect: the center of ESO184-G82 is significantly more chemically-enriched than the outer regions.

Using a linear regression on the data of Figure 8, the metallicity gradient is best fit with a slope of 0.25 ± 0.01 dex/ R_{25} in relative, or 0.056 dex/kpc in physical scales, well in the range that was previously derived for galaxies of comparable stellar mass (Ho et al. 2015; ?). Here, R_{25} is the radius at the $B = 25$ mag arcsec $^{-2}$ isophote. O3N2-based diagnostics return

slightly steeper, but within errors generally compatible values. The linear fit to the oxygen abundance data is a reasonable description of the data, except for the very center below a deprojected distance of 1 kpc, where the metallicity is seen to decrease more steeply. Limiting the fit range to data below 1 kpc, the slope in the central kpc is 0.18 dex/kpc (see dashed line in Figure 8).

A comparison between this metallicity gradient to the typical values of (projected) GRB distances from the galaxy centers of 1.3 kpc (Blanchard et al. 2016) does not provide strong reason to suggest that the average measurement of GRB host metallicities from spatially-unresolved data is significantly skewed when compared to the GRB site metallicity. There is however a non-negligible fraction of GRBs at substantial distances to their hosts (10% at > 3 kpc) where metallicity gradients might lead to overestimates on the GRB site abundance from unresolved spectra.

Figure 8 also illustrates the typical spread of oxygen abundances at a given galactic radius. With an root-mean-square (RMS) spread below 0.1 dex below R_{25} , and we find no evidence for extremely ($Z < 0.1Z_{\odot}$) gas-poor regions at the spatial scales probed by our observation (100 pc).

4.6. ESO184-G82 if Seen at High Redshift

GRB 980425/SN 1998bw is the closest GRB detected in two decades, and an exceptional opportunity to measure the physical parameters of its host within high precision and high spatial resolution. Typically, information on environments of GRBs or similar kind of transients at higher redshift is obtained only through galaxy-integrated measurements (Krühler et al. 2015; Japelj et al. 2016), where it is not necessarily obvious whether the measured parameters actually correspond to GRB/SN location properties. We thus seek to compare the GRB explosion site spectrum extracted from the 9 closest spaxels to a galaxy-integrated spectrum as it would appear if it were unresolved and observed through a long-slit.

First, we compare the total SFR as derived from integrating all spaxels after a reddening correction ($SFR = 0.23 \pm 0.02 M_{\odot} \text{ yr}^{-1}$), to the value what would be inferred from the H α flux corrected from the $E_{B-V} = 0.07 \pm 0.01$ derived from the integrated spectrum ($SFR = 0.18 \pm 0.01 M_{\odot} \text{ yr}^{-1}$). Both values nicely agree with far-infrared, [O I], and [C II] derived SFRs (Michałowski et al. 2014, 2016), and the narrow-band H α image from Sollerman et al. (2005) once their Salpeter IMF is taken into account. The difference to other H α -derived SFR (Hammer et al. 2006; Christensen et al. 2008) is entirely due to their overestimated dust correction and a different IMF.

We then derive physical parameters from the spectra of the explosion site, the central part of the Wolf-Rayet region, and the integrated galaxy within a diameter of 50" around its center as summarized in Table 1. There is good agreement between many of the physical properties of the galaxy and the SN site spectrum. Not unexpectedly, resolved measurement of EWs at the SN site are somewhat higher, whereas both dust (by 0.02 mag) and oxygen abundance (by 0.1 dex) are somewhat lower at the SN site than for a galaxy integrated spectrum. ESO184-G82 thus does not provide strong evidence that GRB position spectra are markedly different from galaxy-integrated values. Whether this observation remains valid for a larger sample of GRB hosts remains to be seen, of course.

Comparing table 1 with Figures 8 and 6 also illustrates that the oxygen abundance derived from a galaxy-integrated spectrum is not the central abundance of the galaxy. As the metallicity determination in an unresolved case is a SFR-weighted measurement, it is dominated by H II-regions primarily located offset

from the center as illustrated in Figure ??, so it corresponds to a distance of around 2 – 3 kpc from the center.

5. Conclusions and Summary

SN1998bw represented the first solid observational evidence that linked GRBs with core-collapse supernovae, and since then has become the prototypical GRB/SN in terms of luminosity as well as spectra and light curve evolution. This SN has already demonstrated the absence of hydrogen and helium as well as broad absorption lines characteristic of a photosphere expanding at high velocities that should become typical of SNe following long GRBs in the later years.

In this article, we use spatially-resolved spectroscopy obtained with the state-of-the art IFU MUSE over 10x10 kpc with individual spaxels covering 35 x 35 pc (effective spatial resolution of 100 pc) to study the properties of the stellar population at the SN position. We show that GRB 980425/SN1998bw exploded in a young (5 - 8 Myr old), dust-poor ($E_{B-V} = 0.03^{+0.06}_{-0.03}$ mag), low-metallicity ($Z \sim 0.2Z_{\odot}$) environment. These ages of the stellar population correspond to life times of stars with ZAMS masses between approximately 25 to 40 M_{\odot} . A similar progenitor mass was derived from modeling the SN 1998bw's nebular spectra (Maeda et al. 2006), and hence provides evidence that the GRB formed in situ.

Empirical strong-line diagnostic ratios based on [O III]/H β and/or [N II]/H α fail to produce accurate maps of oxygen abundance, and we explain this observation through the dependence of the respective diagnostic ratio on ionization. Using a recent method based on photoionization models and [S II] from Dopita et al. (2016), we derive $12 + \log(\text{O}/\text{H}) = 8.06 \pm 0.06$ or $Z = 0.20^{+0.04}_{-0.02} Z_{\odot}$ at the SN position, 8.15 ± 0.01 for a galaxy integrated spectrum and 8.21 ± 0.03 for the nearby WR region. Similar, but somewhat higher (by up to 0.2 dex) values result from electron temperatures via the observed ratio of auroral-to-nebular [S III] or [O III].

Acknowledgements. Its a pleasure to acknowledge D. Malesani for providing broad-band imaging of the SN field.

References

- Allain, D., Collin-Souffrin, S., Joly, M., & Vigroux, L. 1979, A&A, 78, 200
 Amorín, R. O., Pérez-Montero, E., & Vilchez, J. M. 2010, ApJ, 715, L128
 Anderson, J. P., Covarrubias, R. A., James, P. A., Hamuy, M., & Haberman, S. M. 2010, MNRAS, 407, 2660
 Appenzeller, I., Fricke, K., Fürtig, W., et al. 1998, The Messenger, 94, 1
 Asplund, M., Grevesse, N., Sauval, A. J., & Scott, P. 2009, ARA&A, 47, 481
 Bacon, R., Accardo, M., Adjali, L., et al. 2010, in Proc. SPIE, Vol. 7735, Ground-based and Airborne Instrumentation for Astronomy III, 773508
 Banerjee, S., Kroupa, P., & Oh, S. 2012, ApJ, 746, 15
 Binette, L., Matadamas, R., Hägele, G. F., et al. 2012, A&A, 547, A29
 Blanchard, P. K., Berger, E., & Fong, W.-f. 2016, ApJ, 817, 144
 Bruzual, G. & Charlot, S. 2003, MNRAS, 344, 1000
 Chabrier, G. 2003, PASP, 115, 763
 Chen, T.-W., Smartt, S. J., Bresolin, F., et al. 2013, ApJ, 763, L28
 Christensen, L., Vreeswijk, P. M., Sollerman, J., et al. 2008, A&A, 490, 45
 Cid Fernandes, R., Mateus, A., Sodré, L., Stasińska, G., & Gomes, J. M. 2005, MNRAS, 358, 363
 Cid Fernandes, R., Schoenell, W., Gomes, J. M., et al. 2009, in Revista Mexicana de Astronomía y Astrofísica Conference Series, Vol. 35, Revista Mexicana de Astronomía y Astrofísica Conference Series, 127–132
 Clocchiatti, A., Suntzeff, N. B., Covarrubias, R., & Candia, P. 2011, AJ, 141, 163
 Diaz, A. I., Terlevich, E., Vilchez, J. M., Pagel, B. E. J., & Edmunds, M. G. 1991, MNRAS, 253, 245
 Dopita, M. A., Kewley, L. J., Heisler, C. A., & Sutherland, R. S. 2000, ApJ, 542, 224
 Dopita, M. A., Kewley, L. J., Sutherland, R. S., & Nicholls, D. C. 2016, Ap&SS, 361, 61
 Dors, Jr., O. L., Krabbe, A., Hägele, G. F., & Pérez-Montero, E. 2011, MNRAS, 415, 3616
 Eldridge, J. J., Langer, N., & Tout, C. A. 2011, MNRAS, 414, 3501
 Erb, D. K., Shapley, A. E., Pettini, M., et al. 2006, ApJ, 644, 813
 Esteban, C., Peimbert, M., García-Rojas, J., et al. 2004, MNRAS, 355, 229
 Evans, I. N. & Dopita, M. A. 1985, ApJS, 58, 125
 Fagotto, F., Bressan, A., Bertelli, G., & Chiosi, C. 1994, A&AS, 105
 Förster Schreiber, N. M., Genzel, R., Bouché, N., et al. 2009, ApJ, 706, 1364
 Fynbo, J. P. U., Jakobsson, P., Prochaska, J. X., et al. 2009, ApJS, 185, 526
 Fynbo, J. U., Holland, S., Andersen, M. I., et al. 2000, ApJ, 542, L89
 Galama, T. J., Vreeswijk, P. M., van Paradijs, J., et al. 1998, Nature, 395, 670
 Galbany, L., Anderson, J. P., Rosales-Ortega, F. F., et al. 2016a, MNRAS, 455, 4087
 Galbany, L., Stanishev, V., Mourão, A. M., et al. 2014, A&A, 572, A38
 Galbany, L., Stanishev, V., Mourão, A. M., et al. 2016b, A&A, 591, A48
 Graham, J. F. & Fruchter, A. S. 2013, ApJ, 774, 119
 Hammer, F., Flores, H., Schaerer, D., et al. 2006, A&A, 454, 103
 Hjorth, J. & Bloom, J. S. 2012, The Gamma-Ray Burst - Supernova Connection, 169–190
 Ho, I.-T., Kudritzki, R.-P., Kewley, L. J., et al. 2015, MNRAS, 448, 2030
 Hoogerwerf, R., de Bruijne, J. H. J., & de Zeeuw, P. T. 2001, A&A, 365, 49
 Iwamoto, K., Mazzali, P. A., Nomoto, K., et al. 1998, Nature, 395, 672
 Izotov, Y. I., Stasińska, G., Meynet, G., Guseva, N. G., & Thuan, T. X. 2006, A&A, 448, 955
 Izotov, Y. I. & Thuan, T. X. 1999, ApJ, 511, 639
 Japelj, J., Vergani, S. D., Salvaterra, R., et al. 2016, A&A, 590, A129
 Kann, D. A., Schady, P., Olivares E., F., et al. 2016, A&A, submitted [arXiv:1606.06791]
 Kashino, D., Renzini, A., Silverman, J. D., & Daddi, E. 2016, ApJ, 823, L24
 Kennicutt, Jr., R. C. 1998, ARA&A, 36, 189
 Kewley, L. J. & Dopita, M. A. 2002, ApJS, 142, 35
 Kewley, L. J. & Ellison, S. L. 2008, ApJ, 681, 1183
 Kobulnicky, H. A. & Kewley, L. J. 2004, ApJ, 617, 240
 Krühler, T., Fynbo, J. P. U., Geier, S., et al. 2012, A&A, 546, A8
 Krühler, T., Malesani, D., Fynbo, J. P. U., et al. 2015, A&A, 581, A125
 Kulkarni, S. R., Frail, D. A., Wieringa, M. H., et al. 1998, Nature, 395, 663
 Kuncarayakti, H., Doi, M., Aldering, G., et al. 2013, AJ, 146, 30
 Kuncarayakti, H., Galbany, L., Anderson, J. P., Krühler, T., & Hamuy, M. 2016, A&A, in press [arXiv:1607.03446]
 Lauberts, A. & Valentijn, E. A. 1989, The surface photometry catalogue of the ESO-Uppsala galaxies
 Leloudas, G., Gallazzi, A., Sollerman, J., et al. 2011, A&A, 530, A95
 Leloudas, G., Schulze, S., Krühler, T., et al. 2015, MNRAS, 449, 917
 Levesque, E. M., Berger, E., Soderberg, A. M., & Chornock, R. 2011, ApJ, 739, 23
 Levesque, E. M. & Leitherer, C. 2013, ApJ, 779, 170
 Li, W., Leaman, J., Chornock, R., et al. 2011, MNRAS, 412, 1441
 López-Sánchez, Á. R., Dopita, M. A., Kewley, L. J., et al. 2012, MNRAS, 426, 2630
 Lunnan, R., Chornock, R., Berger, E., et al. 2014, ApJ, 787, 138
 Maeda, K., Nomoto, K., Mazzali, P. A., & Deng, J. 2006, ApJ, 640, 854
 Maiolino, R., Nagao, T., Grazian, A., et al. 2008, A&A, 488, 463
 Marino, R. A., Rosales-Ortega, F. F., Sánchez, S. F., et al. 2013, A&A, 559, A114
 Mazzali, P. A., Nomoto, K., Patat, F., & Maeda, K. 2001, ApJ, 559, 1047
 McGaugh, S. S. 1991, ApJ, 380, 140
 Mendoza, C. & Zeppen, C. J. 1982, MNRAS, 199, 1025
 Meynet, G. & Maeder, A. 2005, A&A, 429, 581
 Michałowski, M. J., Castro Ceron, J. M., Wardlow, J. L., et al. 2016, ArXiv e-prints [A&A, in press, arXiv:1609.01742:1609.01742]
 Michałowski, M. J., Hjorth, J., Malesani, D., et al. 2009, ApJ, 693, 347
 Michałowski, M. J., Hunt, L. K., Palazzi, E., et al. 2014, A&A, 562, A70
 Modjaz, M., Kewley, L., Bloom, J. S., et al. 2011, ApJ, 731, L4
 Morisset, C., Delgado-Inglada, G., Sánchez, S. F., et al. 2016, A&A, 594, A37
 Nagao, T., Maiolino, R., & Marconi, A. 2006, A&A, 459, 85
 Nicholls, D. C., Dopita, M. A., & Sutherland, R. S. 2012, ApJ, 752, 148
 Nicholls, D. C., Dopita, M. A., Sutherland, R. S., Kewley, L. J., & Palay, E. 2013, ApJS, 207, 21
 Osterbrock, D. E. 1989, Astrophysics of gaseous nebulae and active galactic nuclei
 Osterbrock, D. E. & Ferland, G. J. 2006, Astrophysics of gaseous nebulae and active galactic nuclei
 Pagel, B. E. J., Edmunds, M. G., Blackwell, D. E., Chun, M. S., & Smith, G. 1979, MNRAS, 189, 95
 Patat, F., Cappellaro, E., Danziger, J., et al. 2001, ApJ, 555, 900
 Peimbert, A. 2003, ApJ, 584, 735
 Peimbert, M. 1967, ApJ, 150, 825
 Pellegrini, E. W., Baldwin, J. A., & Ferland, G. J. 2011, ApJ, 738, 34
 Perets, H. B. & Šubr, L. 2012, ApJ, 751, 133
 Pérez-Montero, E., Contini, T., Lamareille, F., et al. 2013, A&A, 549, A25

Table 1: GRB 980425/SN 1998bw properties from extracted spectra

	ESO184-G82	SN region	WR region
EW(H α) (Å)	56.0 \pm 1.4	82 \pm 2	> 900
EW([O III]) (Å)	34.5 \pm 0.9	50 \pm 2	> 850
E_{B-V} (mag)	0.07 \pm 0.01	0.05 \pm 0.02	0.21 \pm 0.01
n_e (cm $^{-3}$)	80 \pm 10	90 \pm 10	140 \pm 10
T_e ([S III]) (10 4 K) ^(a)	...	1.24 \pm 0.18	0.93 \pm 0.01
T_e ([O III]) (10 4 K) ^(a)	...	1.29 \pm 0.18	1.05 \pm 0.05
12 + log(O/H) (D16) ^(a)	8.15 \pm 0.01	8.06 \pm 0.01	8.21 \pm 0.01
12 + log(O/H) (PP04, O3N2) ^(a)	8.32 \pm 0.01	8.31 \pm 0.01	8.11 \pm 0.01
12 + log(O/H) (PP04, N2) ^(a)	8.34 \pm 0.01	8.32 \pm 0.01	8.19 \pm 0.01
12 + log(O/H) (T_e)	...	\sim 8.1	\sim 8.3
SFR (M_\odot yr $^{-1}$)	0.23 \pm 0.02

Notes. ^(a) The quoted error is statistical only. There is an additional systematic error in each of these measurements due to various reasons. For the respective parameters, it is approximately $T_e = 0.1 \cdot 10^4$ K, 12 + log(O/H) (PP04, O3N2)=0.14 dex, 12 + log(O/H) (PP04, N2)=0.18 dex. The systematic error on 12 + log(O/H) (D16) is presently not well quantified, but we expect it in the range of \sim 0.1 dex.

Perley, D. A., Quimby, R., Yan, L., et al. 2016, ArXiv e-prints [arXiv:1604.08207]
Pettini, M. & Pagel, B. E. J. 2004, MNRAS, 348, L59
Pilyugin, L. S. & Thuan, T. X. 2005, ApJ, 631, 231
Planck Collaboration. 2014, A&A, 571, A16
Prieto, J. L., Krühler, T., Anderson, J. P., et al. 2016, ApJL, in press [arXiv:1609.00013]
Prieto, J. L., Stanek, K. Z., & Beacom, J. F. 2008, ApJ, 673, 999
Sánchez, S. F., Rosales-Ortega, F. F., Iglesias-Páramo, J., et al. 2014, A&A, 563, A49
Schady, P., Krühler, T., Greiner, J., et al. 2015, A&A, 579, A126
Schlafly, E. F. & Finkbeiner, D. P. 2011, ApJ, 737, 103
Sollerman, J., Östlin, G., Fynbo, J. P. U., et al. 2005, New A, 11, 103
Soto, K. T., Lilly, S. J., Bacon, R., Richard, J., & Conseil, S. 2016, MNRAS, 458, 3210
Stasińska, G. 2006, A&A, 454, L127
Storey, P. J. & Zeippen, C. J. 2000, MNRAS, 312, 813
Thöne, C. C., Christensen, L., Prochaska, J. X., et al. 2014, MNRAS, 441, 2034
Thöne, C. C., de Ugarte Postigo, A., García-Benito, R., et al. 2015, MNRAS, 451, L65
Thöne, C. C., Fynbo, J. P. U., Östlin, G., et al. 2008, ApJ, 676, 1151
Tremonti, C. A., Heckman, T. M., Kauffmann, G., et al. 2004, ApJ, 613, 898
Weilbacher, P. M., Streicher, O., Urrutia, T., et al. 2014, in Astronomical Society of the Pacific Conference Series, Vol. 485, Astronomical Data Analysis Software and Systems XXIII, ed. N. Manset & P. Forshay, 451
Wesson, R., Stock, D. J., & Scicluna, P. 2016, MNRAS, 459, 3475
Wiersema, K., Savaglio, S., Vreeswijk, P. M., et al. 2007, A&A, 464, 529
Xu, D., de Ugarte Postigo, A., Leloudas, G., et al. 2013, ApJ, 776, 98
Zaritsky, D., Kennicutt, Jr., R. C., & Huchra, J. P. 1994, ApJ, 420, 87
Zeh, A., Klose, S., & Hartmann, D. H. 2004, ApJ, 609, 952

Appendix A: Re-analysis of Archival Long-slit Spectra

The ESO archive contains a number of low-resolution spectra obtained with the FOcal Reducer/low dispersion Spectrograph 2 (FORS2, Appenzeller et al. 1998) that are particularly interesting in the context of this work. These are the same spectra used by Hammer et al. (2006), and contain data taken with a 1''0 slit on 2004-07-15 with the grism 600B (3450 Å to 6050 Å with resolving power $R \sim 850$) and on 2004-07-16 in grism 600RI (5300 Å to 8450 Å with $R \sim 1050$). The position angle during both observations was 28° from East such that both the SN and WR region are covered by the slit (Figure 1). The total exposure time was 1350 s (each three individual frames with 300 s and 150 s) in the 600B setup and 2250 s in the 600RI (each five single frames with 300 s and 150 s) setup. We reduce and analyse this archival FORS2 data using standard procedures, specifically

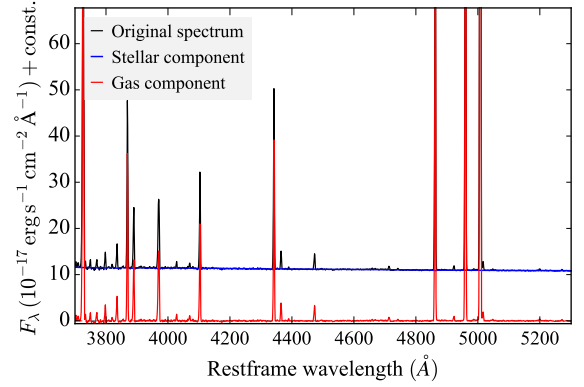


Fig. A.1: FORS2 600B spectrum of the brightest pixel of the WR region. Black is the original spectrum, blue the fitted stellar component, and red the resulting spectrum for the gas-phase only. Blue and black spectra are shifted to enhance clarity in the Figure.

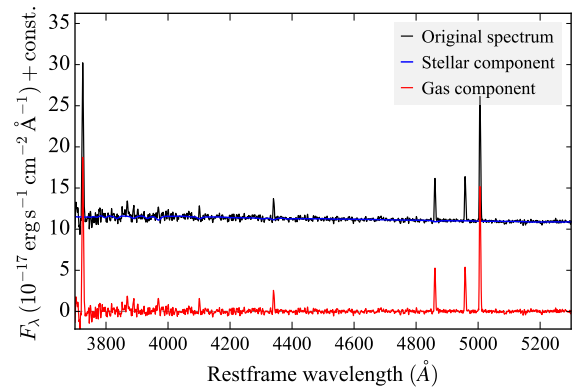


Fig. A.2: FORS2 600B spectrum of the explosion site. Black is the original spectrum, blue the fitted stellar component, and red the resulting spectrum for the gas-phase only. Blue and black spectra are shifted to enhance clarity in the Figure.

the ESO FORS2 pipeline in its version 5.3.8 and self-written methods and algorithms in python (Krühler et al. 2015).

In particular the 600B data are taken under excellent atmospheric conditions leading to a width of the spectral line spread function of $\text{FWHM}=0.6$ at 5000 \AA as evidenced by the trace of a stellar source serendipitously on the slit at a distance of $22''.0$ to the WR region. The 600RI data have somewhat worse spatial resolution ($\text{FWHM}=1''.0$ at 7000 \AA). This mismatch leads to the complication that the two different spectra are convolved with very different spatial scales. Due to the small angular size of the of WR region core ($\lesssim 0''.1$ via HST imaging), and the gradient in physical properties, ratios of lines observed in the two different setups (e.g. for dust reddening distribution) are thus clearly non-trivial to interpret.

Table A.1 contains line fluxes and equivalent widths from our analysis of the FORS spectra, sometimes significantly different to the Hammer et al. (2006) values. No error is given for the line fluxes there, but a substantial uncertainty by at least 25% must be present (as estimated from the apparent discrepancy between their line-flux ratios of $[\text{O III}](\lambda 5007)/[\text{O III}](\lambda 4959)$ and $[\text{N II}](\lambda 6584)/[\text{N II}](\lambda 6548)$ to the theoretical value of 2.98 set by magnetic-dipole transition probabilities and observed in high-quality SDSS spectra (e.g. Storey & Zeippen 2000; Osterbrock & Ferland 2006; Wesson et al. 2016).

From the $\text{H}\beta/\text{H}\gamma$ and $\text{H}\beta/\text{H}\delta$ ratio, we derive an $E_{B-V} = 0.22 \pm 0.03$ mag for the WR and $E_{B-V} = 0.08^{+0.23}_{-0.08}$ mag for the SN region, both perfectly consistent with the MUSE data⁶. Also other properties are very similar to our IFU-based values as given in Table 1.

We finally use the blue response of the FORs 600B grism to derive an age of the H II region through a fit using composite stellar templates in *starlight* in a similar manner as in the main text. The stellar population in the WR region is extremely young, and the Bruzual & Charlot (2003) template with an age of 1 Myr dominates the best fit by contributing ~ 60 -90% to the total observed star light in various fits using different template bases and reddening laws. This very young age is consistent with the extremely high EW of $[\text{O III}]$ and $\text{H}\alpha$ (Table A.1), and the age constraints derived in the main text.

The SN region has prominent stellar components with ages of 5 Myr and 40 Myr (each contributing around 30% to the best-fit composite template), the younger of which is again consistent with the age estimate from the $\text{H}\alpha$ EW in the main text.

Appendix B: Dependence of O3N2-derived Oxygen Abundance on Ionization Parameter

To better illustrate how a changing ionization parameter affects the metallicity measurement in the O3N2 or N2-scales we show in Figure C.1 the ionization parameter U (defined as ionizing photons per hydrogen atoms) versus $12 + \log(\text{O}/\text{H})$ in the Pettini & Pagel (2004) or Dopita et al. (2016) scale of the brightest H II -region in ESO184-G82. Here, we use the $[\text{S II}]/[\text{S III}]$ ratio (Figure 5) to calculate U via photo-ionization models (Dors et al. 2011). Different parametrizations in U (e.g. Morisset et al. 2016) do not change Figure C.1 significantly. The $[\text{S II}]/[\text{S III}]$ ratio has the advantage of being nearly insensitive to metallicity, so we should not see a strong correlation between both quantities in accurate metallicity diagnostics. It is again clear, however, that the O3N2-based metallicity scale only reproduces the H II -region metallicity in spaxels with low ionization parameter, and systematically under-predicts it at higher U . In contrast, the Dopita

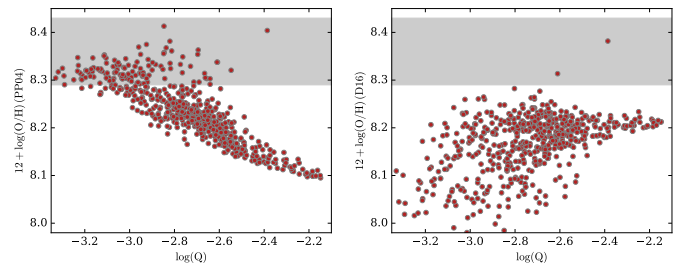


Fig. B.1: Dependence of the inferred abundance in two scales (left: Pettini & Pagel 2004, right: Dopita et al. 2016) on the ionization parameter U for the WR region. Each data point corresponds to a single spaxel, and the grey region indicates the metallicity constraints from the temperature-sensitive $[\text{O III}](\lambda 4363)$.

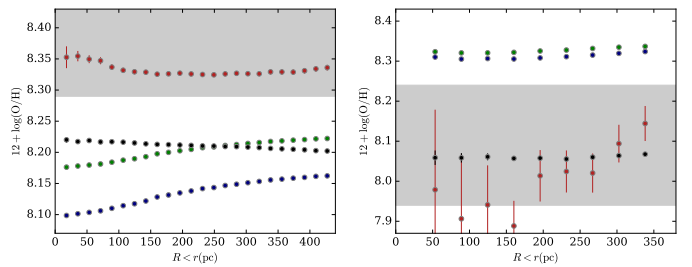


Fig. C.1: Abundances inferred when integrating over H II -regions as illustrated by a high- and low-ionization region (the WR-region in the left, and the SN-region in the right plot, respectively). The x-axis shows the radius over which we integrate spaxels to derive the oxygen abundance (y-axis). The grey shaded area shows the allowed range from abundance derived using the temperature-sensitive $[\text{O III}](\lambda 4363)$ line.

et al. (2016) diagnostic is mostly independent on ionization parameter, but seems offset by an average ~ 0.15 dex towards lower oxygen abundances (Figure C.1, lower panel).

Appendix C: H II -region Integrated Abundances

It is worth keeping in mind that the original calibration of the O3N2 strong-line diagnostic ratio is obtained on H II -region integrated spectra, while our MUSE data spatially resolve the ionized gas, in particular around the brightest star-forming regions. To maintain consistency with the diagnostic, previous authors have thus synthesized average spectra from their IFU data by adding up spaxels that had previously been identified to belong to individual H II -regions. This procedure assumes that all H II -regions have a similar ionization structure consistent with the calibration sample of the diagnostic. Figure C.1 shows the evolution of the O3N2-based abundance when integrating spaxels with an increasingly large distance from the center of the H II -region for the WR region and GRB explosion site.

⁶We would measure significant dust reddening if we would not correct our $\text{H}\beta$, $\text{H}\gamma$, or $\text{H}\delta$ fluxes for stellar Balmer absorption

Table A.1: GRB 980425/SN 1998bw fluxes/EW from long-slit spectra

	SN region ^a		WR region ^b	
	Flux ^c	EW _{rest} (Å)	Flux ^c	EW _{rest} (Å)
[O II](λ3727)	47 ± 2	48 ± 3	41 ± 3	250 ± 5
[Ne III](λ3968)	4.3 ± 0.6	3.1 ± 0.9	8.2 ± 0.2	52 ± 2
Hδ	2.6 ± 0.5	3.6 ± 0.8	7.7 ± 0.2	51 ± 2
Hγ	5.6 ± 0.5	9.0 ± 1.2	14.7 ± 0.3	57 ± 3
[O III](λ4363)	0.6 ± 0.2	2.2 ± 0.8	1.54 ± 0.05	10 ± 1
Hβ	12.4 ± 1.1	24 ± 2	34.6 ± 1.4	313 ± 3
[O III](λ4959)	12.9 ± 1.2	24 ± 2	68 ± 2	650 ± 5
[O III](λ5007)	40 ± 2	75 ± 4	205 ± 4	1980 ± 20
[N II](λ6548) ^b	1.3 ± 0.2	5.0 ± 1.0	1.57 ± 0.03	25 ± 1
Hα	38.5 ± 1.6	115 ± 6	77 ± 2	1220 ± 20
[N II](λ6584)	4.9 ± 0.3	15.9 ± 1.8	4.7 ± 0.2	79 ± 3
[S II](λ6717)	7.8 ± 0.3	29 ± 2	4.4 ± 0.2	87 ± 3
[S II](λ6731)	5.9 ± 0.3	20 ± 2	3.4 ± 0.3	70 ± 3

Notes. ^(a) To increase the S/N ratio, we include the adjacent two pixels in the extraction for the SN region. ^(b) Derived from the spectrum at the peak of the emission of the WR region. ^(c) Fluxes are given as 10^{-16} erg s⁻¹ cm⁻². ^(d) The double horizontal line separates the nebular lines that were taken in the two different FORS2 setups. Due to the different width of the line spread function and thus angular scales observed in both setups, the lines below and above the horizontal line cannot easily be used together to infer physical properties.